

1 **TITLE:**

2 Inference of recombination maps from a single pair of genomes and its application
3 to archaic samples

4

5 **AUTHORS:** Gustavo V. Barroso*¹, Natasa Puzovic¹ and Julien Y. Dutheil^{1,2}

6

7 **Affiliations:**

8 1) Max Planck Institute for Evolutionary Biology. Department of Evolutionary Genetics.

9 August-Thienemann-Straße 2 24306 Plön – GERMANY

10 2) ISEM – Institut des Sciences de l'Évolution. UMR 5554, Université de Montpellier, Place

11 Eugène Bataillon 34095 Montpellier cedex 05 – FRANCE

12

13 **Corresponding Author:**

14 *Gustavo V. Barroso, Max Planck Institute for Evolutionary Biology. Department of

15 Evolutionary Genetics. August-Thienemann-Straße 2, 24306 Plön – GERMANY.

16

17

18 **ABSTRACT:**

19 Understanding the causes and consequences of recombination rate evolution is a fundamental
20 goal in genetics that requires recombination maps from across the tree of life. Since statistical
21 inference of recombination maps typically depends on large samples, reaching out studies to
22 non-model organisms requires alternative tools. Here we extend the sequentially Markovian
23 coalescent model to jointly infer demography and the variation in recombination along a pair of
24 genomes. Using extensive simulations and sequence data from humans, fruit-flies and a fungal
25 pathogen, we demonstrate that iSMC accurately infers recombination maps under a wide range
26 of scenarios – remarkably, even from a single pair of unphased genomes. We exploit this
27 possibility and reconstruct the recombination maps of archaic hominids. We report that the
28 evolution of the recombination landscape follows the established phylogeny of Neandertals,
29 Denisovans and modern human populations, as expected if the genomic distribution of cross-
30 overs in hominids is largely neutral.

31 Meiotic recombination is a major driver of the evolution of sexually-reproducing species¹. The
32 crossing-over of homologous chromosomes creates new haplotypes and breaks down linkage
33 between neighbouring loci, thereby impacting natural selection^{2,3} and consequently the genome-
34 wide distribution of diversity⁴. The distribution of such cross-over events is heterogeneous within
35 and among chromosomes^{5,6}, and commonly referred to as the recombination landscape – a
36 picture of how often genetic variation is shuffled in different parts of the genome. Interestingly,
37 this picture is not static, but instead is an evolving trait that varies between populations^{7,8} and
38 species⁹. Moreover, the proximate mechanisms responsible for shaping the recombination
39 landscape vary among *taxa*. For example, among primates (where the PRDM9 gene is a key
40 player determining the location of so-called recombination hotspots¹⁰) the landscape is conserved
41 at the mega-base (Mb) scale, but not at the kilo-base (kb) scale¹¹. In birds, which lack PRDM9,
42 the hotspots are found near transcription start sites in the species that have been studied so far^{8,12}.
43 In *Drosophila* (where clear hotspots appear to be absent¹³), inter-specific changes are associated
44 with mei-218 variants¹⁴, a gene involved in the positioning of double-strand breaks¹⁵. The
45 molecular machinery influencing the distribution of cross-over events is still poorly understood
46 in many other groups, where a picture of the recombination landscape in closely related species
47 is lacking.

48

49 Aside from their intrinsic value in genetics, accurate recombination maps are needed to interpret
50 the distribution of diversity along the genome. Since the rate of recombination determines the
51 extent to which linked loci share a common evolutionary history¹⁶, inferring selection¹⁷⁻¹⁹,
52 introgression^{18,20} and identifying causal loci in association studies requires knowledge of the
53 degree of linkage between sites²¹. Furthermore, recombination can cause GC-biased gene
54 conversion^{22,23}, which can mimic the effect of selection²⁴ or interfere with it²⁵. Obtaining
55 recombination maps, however, remains a challenging task. Due to the typically low density of
56 markers, experimental approaches provide broad-scale estimates and are limited in the number of

57 amenable *taxa*. Conversely, population genomic approaches based on coalescent theory^{26,27} have
58 proved instrumental in inferring recombination rates from polymorphism data.

59

60 Traditionally, population genomic methods infer recombination maps from variation in linkage
61 disequilibrium (LD) between pairs of single nucleotide polymorphisms (SNPs)^{28–30}. However,
62 since “LD-based” methods typically require large sample sizes per population (from a dozen
63 individuals³¹), their application is restricted to a few model organisms where such sequencing
64 effort could be afforded. Moreover, because computation of the exact likelihood is intractable for
65 long sequences, the underlying model only accounts for pairs of SNPs³², multiple pairs being
66 considered independent and combined using a composite likelihood approach. To avoid over-
67 fitting due to the high number of parameters, smoothness in the landscape is enforced by using
68 heuristic corrections that have been fine-tuned for humans²⁸ or fruit-flies³⁰. Application of these
69 methods to systems with distinct genomic architectures therefore requires extra-benchmarking
70 (see for instance Stukenbrock and Dutheil³¹).

71

72 Here we introduce a new modeling framework (iSMC) to infer the variation in the recombination
73 rate along the genome, using a single pair of unphased genomes. Using simulations, we show
74 that iSMC is able to accurately recover the recombination landscape under diverse scenarios. We
75 further demonstrate its efficacy with case studies in Humans, Fruit-flies and the fungal pathogen
76 *Zymoseptoria tritici*, where experimental genetic maps are available. Finally, we exploit our new
77 method to investigate the recombination landscape of archaic hominid samples: Ust’Ishim, the
78 Vindija Neandertal, the Altai Neandertal and the Denisovan. Because it allows inference from
79 datasets for which sample size is intrinsically limited, such as ancient DNA samples, our method
80 opens a new window in the study of the recombination landscape evolution.

81

82 **RESULTS:**

83 Overview of iSMC

84 Besides its common interpretation as a backwards-in-time process, the coalescent with
85 recombination^{33,34} can also be modelled as unfolding spatially along chromosomes³⁵. Starting
86 from a genealogy at the first position of the alignment, the process moves along the chromosome
87 sequence, adding recombination and coalescence events to the ensuing ancestral recombination
88 graph (ARG)^{36,37} (**Figure 1a**). Due to long-range correlations imposed by rare recombination
89 events that happen outside the ancestry of the sample (in so-called trapped non-ancestral
90 material³⁸), the genealogy after a recombination event cannot be entirely deduced from the
91 genealogy before, rendering the process non-Markovian. The sequentially Markovian coalescent
92 process (SMC)^{39,40} ignores such recombination events, but captures most of the properties of the
93 original coalescent⁴¹ while being computationally tractable. It is the foundation of recent models
94 for demographic inference⁴²⁻⁴⁴ and has been used to infer the broad-scale recombination map of
95 the human-chimpanzee ancestor based on patterns of incomplete lineage sorting^{45,46}. In the SMC,
96 transition probabilities between genealogies are functions of ancestral coalescence rates and – of
97 key relevance to this study – the population recombination rate ($\rho = 4.Ne.r$)^{43,44}. Thus,
98 heterogeneous recombination landscapes affect the SMC by modulating the frequency of
99 genealogy transitions: genomic regions with higher recombination rate are expected to harbour
100 relatively more genealogies than regions with smaller recombination rate (**Figure 1**). We
101 leverage this information by extending the SMC to accommodate spatial heterogeneity in ρ (see
102 Methods). In brief, our new model combines the discretised distribution of times to the most
103 recent common ancestor (TMRCAs) of the pairwise SMC⁴³ with a discretised distribution of ρ to
104 jointly model their variation along the genome. Since we model the transition between
105 discretised ρ categories as a spatially Markovian process along the genome, combining the SMC
106 with the Markov model of recombination variation leads to a Markov-modulated Markov model.
107 We cast it as a hidden Markov model^{47,48} (HMM) to generate a likelihood function, where the
108 observed states are orthologous nucleotides and the hidden states are {TMRCA, ρ -category}

109 pairs (**Figure 1c**). We name our new approach “integrative sequentially Markov coalescent
110 (iSMC)”, as it enables jointly capturing the effect of time and space in the Coalescent. This
111 framework explicitly connects the genealogical process with the classical definition of LD as the
112 non-random association of alleles at different loci⁴⁹, which has been formulated in terms of
113 covariances in coalescence times⁵⁰. Henceforth, we restrict the use of the term LD to its
114 “topological” interpretation⁵¹.

115

116 iSMC models spatial variation in the recombination rate using a single discrete distribution
117 (**Figure 1b**), which can be accommodated to various models of recombination rate variation (see
118 Methods). After fitting the alternative distributions to sequence data, Akaike's Information
119 Criterium (AIC)⁵² is employed as a mean of model selection. If AIC favours a spatially
120 heterogeneous model over the null model where ρ is constant along the genome, iSMC then
121 estimates a recombination landscape of single-nucleotide resolution by weighting the discretised
122 values of the selected distribution with their local posterior probabilities. In the following
123 section, we benchmark our model on different simulated scenarios. The correlations between
124 simulated and inferred maps reported therein were computed after binning the inferred
125 landscapes into windows of 50 kb, 200 kb, 500 kb and 1 Mb.

126

127 **Simulation study**

128 To assess iSMC's overall performance, we used SCR⁵³ to simulate five recombination
129 landscapes corresponding to different patterns of magnitude and frequency of change in ρ and a
130 “null” scenario with constant recombination rate along the genome (see Methods). For each
131 landscape, we simulated 10 ARGs, each describing the ancestry of 2 haploid chromosomes. We
132 tested two discretisation schemes for the joint distribution of TMRCAs and recombination rates:
133 the first with 40 time intervals, five ρ categories; the second with 20 time intervals, 10 ρ
134 categories, leading to a total of 200 hidden states in both configurations (**Supplemental Note**).

135 Model selection based on AIC favours the correct model in 45 of the 50 datasets (**Table S1**),
136 with the five exceptions belonging to the scenario where changes are frequent and of small
137 magnitude. In this regime, transitions to regions of slightly different recombination rates do not
138 significantly skew the distribution of genealogies, and the short length of blocks with constant ρ
139 leaves little signal in the data. Nevertheless, correlations between simulated and inferred maps
140 are highly significant (ranging from 0.385 to 0.563 in the five identifiable replicates with
141 frequent changes of low magnitude, and from 0.682 to 0.928 in the others, **Tables S2, S3**).
142 Overall, the results are consistent between replicates and robust to the choice of discretisation
143 (**Figure 2b**). We use the configuration with 40 time intervals and five ρ categories, as it
144 implements a finer discretisation of time that is more adequate to capture the effect of ancestral
145 demography. In the following, as we introduce new simulated scenarios, we focus on the
146 recombination landscape with frequent changes of large magnitude.

147

148 *Demographic history.* The random sampling of haplotypes during population bottlenecks and
149 expansions affects LD between SNPs, thus creating spurious signals of variation in ρ ⁵⁴⁻⁵⁶. To test
150 whether iSMC could capture the effect of demography on the inference of recombination maps,
151 we simulated a heterogeneous recombination landscape coupled with either a recent 20-fold
152 increase, or ancient 20-fold decrease in population size. We then fit our model twice for each
153 scenario: first, erroneously assuming a flat demographic history; second, allowing iSMC to infer
154 piecewise constant coalescence rates in order to accommodate population size changes. The
155 correlation coefficients are all highly significant (**Figure 3**), showing that the inferred
156 recombination landscape is relatively robust to misspecification of the demographic scenario, but
157 are systematically higher when demography is jointly inferred (**Figure 2c-d, Table S4, S5**). The
158 difference is stronger at the fine scale, where, in the presence of complex demography the
159 distribution of genealogies can get locally confined to a time period, and ignorance about
160 differential coalescence rates reflects poorly on local ρ estimates. We conclude that the joint-

161 inference approach of iSMC can disentangle the signal that variable recombination and

162 fluctuating population sizes leave on the distribution of SNPs.

163

164 *Introgression events.* Recent studies suggested that introgression is a frequent phenomenon in

165 nature^{57,58}. The influx of a subset of chromosomes from a source population into another, target

166 population (in a process analogous to a genetic bottleneck) introduces long stretches of SNPs in

167 strong LD. Past introgression events will thus affect runs of homozygosity, potentially biasing

168 the distribution of genealogies. To test the robustness of iSMC to the confounding effect of

169 introgression, we simulated two scenarios of admixture which differ in their time of secondary

170 contact between populations. The correlations between simulated and inferred recombination

171 maps remain highly significant (ranging from 0.631 to 0.834, **Figure 2e**, **Table S6**, **S7**) and

172 depend on the time when introgression occurred. Recombination maps are less accurately

173 recovered in case of recent introgression, because in such case there has been less time for

174 recombination to break SNP associations that do not reflect local ρ in the target, sampled

175 population.

176

177 *Variation in mutation rate.* The rate of *de novo* mutations varies along the genome of many

178 species. For example, CpG di-nucleotides experience an increase in mutation rate (μ) as a result

179 of methylation followed by deamination into thymine, whereas the efficiency of the molecular

180 repair machinery is negatively correlated with the distance from the DNA replication origin,

181 causing μ to vary accordingly⁵⁹. Such heterogeneity could bias iSMC's estimates because the

182 transition into a region of higher μ mimics the transition to a genealogy with a more ancient

183 common ancestor, since in both cases the outcome is locally increased genetic diversity. To

184 assess the impact of variation of mutation rate on the estimation of recombination rate, we

185 simulated two scenarios of variation of $\theta = 4.Ne.\mu$ along the genome, corresponding to low and

186 high frequency of change, relative to the frequency of change in the recombination rate. We

187 report that transitions to different mutation rates along the genome globally do not introduce
188 substantial biases in our estimates (correlations range from 0.655 to 0.844, **Figure 2f**, **Table S8**,
189 **S9**). There is, however, an effect of the local ratio θ / ρ at the fine-scale: regions with a ratio < 1
190 tend to have their local ρ underestimated because the relatively small number of mutations render
191 some recombination events undetectable (**Figure S1a**). Importantly, this effect is a consequence
192 of the magnitude of μ , and is not expected as a result of the local reduction in diversity caused by
193 selection, since in the latter case there is a linear scaling of both θ and ρ (due to a decrease in the
194 local effective population size, N_e), keeping their ratio constant. Furthermore, the bias is reduced
195 when site-specific recombination estimates are binned into larger windows (**Figure S1b**).

196

197 **Application to a fungal pathogen, fruit-flies and humans**

198 We benchmarked iSMC on model organisms with contrasting genomic architectures and
199 evolutionary histories. The leaf blotch *Zymoseptoria tritici* is a highly polymorphic fungal
200 pathogen with a compact genome (40 Mb) that is under widespread selection⁶⁰ and exhibits an
201 extremely rugged recombination landscape^{31,61}. In this species, AIC favours a heterogeneous
202 model with the presence of recombination hotspots in all three pairs of genomes analysed (**Table**
203 **1**, see Methods). Under this model, correlations between iSMC maps and a previously published
204 genetic map⁶¹ are highly significant (**Table S10**) at the 20 kb scale (0.279, 0.287 and 0.308) and
205 increase at the 100 kb scale (0.393, 0.476 and 0.499). In sharp contrast to *Z. tritici*, the
206 recombination landscape in *Drosophila* is notably smooth¹³, and AIC favours a heterogeneous
207 model based on a Gamma distribution. Under this model, correlations between iSMC maps and a
208 genetic map of this species are highly significant (**Table S10**) at the 100 kb scale (0.334, 0.342
209 and 0.363), and increase at the 1 Mb scale (0.549, 0.613 and 0.644). Like in *Zymoseptoria tritici*,
210 model fitting in humans favours a heterogeneous distribution of recombination rates with the
211 presence of hotspots (**Table 1**). We inferred recombination maps under this model for each of the
212 three Yoruban (African), three Dai Chinese (Asian) and three Finnish (European) genomes

213 available in the Simons Genome Diversity Project⁶², and correlated them to the sex-averaged
214 genetic map from DECODE⁷, after binning into windows of 50 kb, 200 kb, 500 kb, and 1 Mb
215 (**Table 2, Table S11**). Correlations between the DECODE map and iSMC maps from the
216 African individuals (range from 0.116 to 0.388 depending on window size) are lower than when
217 individual maps from either Asia (0.177 to 0.457) or Europe (0.179 to 0.455) are compared. This
218 was expected since the DECODE map was estimated from a pedigree study of the Icelandic
219 population. The correlations increase if we use consensus maps (defined here as the average
220 maps among three diploids) from each population (from 0.177 to 0.431 according to window size
221 for Africans, 0.251 to 0.508 for Asians and 0.253 to 0.521 for Europeans). Taken together these
222 results show that iSMC can infer recombination maps from species with extremely different
223 recombination profiles.

224

225 **Application to archaic samples**

226 At the fine scale, the location of cross-over events in great apes is strongly influenced by the
227 sequence of the PRDM9 gene^{6,10,63}. Recombination hotspots determined by PRDM9 tend to erode
228 over time, being replaced somewhere else in the genome with the rise of new PRDM9 alleles.
229 Such turn-over of hotspot locations leads to rapid evolution of the recombination landscape^{64,65},
230 therefore, if the location of hotspots is selectively neutral, recombination maps should become
231 more dissimilar with increasing divergence between populations and species. This hypothesis has
232 been corroborated by two lines of evidence. First, comparisons between recombination maps of
233 extant great ape species show no overlap of hotspots at the fine scale, but correlations increase
234 with window size. While this observation suggests that molecular players other than PRDM9
235 shape the landscape at the large scale, such positive relationship could be an artefact of reduced
236 variance when recombination estimates are averaged in larger windows (e.g., correlations
237 increase with window size in our simulations, despite recombination landscape being static over
238 time, **Table S1-2**). Second, *in silico* prediction of PRDM9 binding sites in the Denisovan

239 genome has shown no overlap of hotspots with modern humans⁶⁶. iSMC's unique ability to
240 extract information from single diploids allowed for an alternative test of this hypothesis through
241 the analyses of four archaic samples⁶⁷: the Altai Neandertal⁶⁸, the Vindija Neandertal⁶⁹, the
242 Denisovan⁷⁰ and the Ust'Ishim individual⁷¹, a 45,000-year-old modern human from Siberia. Pair-
243 wise correlations between individual maps at the fine (50 kb) scale reveals that the evolution of
244 the recombination landscape recapitulates the evolutionary history of hominids: Asians and
245 Europeans form a distinct cluster; the 45,000 year-old Ust'Ishim is a long branch, sister to this
246 clade, depicting similarities in the recombination landscape that have been frozen by his demise
247 soon after the out-of-Africa migration; and all modern humans are highly diverged from the
248 monophyletic Neandertal-Denisovan group (**Figure 4a**). The tree has high bootstrap support for
249 its branches and is corroborated by principal component analysis (**Figure 4b**). Overall, the
250 topology is consistent at larger scales (**Figure S2**), with the notable exception of Ust'Ishim
251 forming a highly supported cluster with the Altai Neandertal. Interestingly, introgression from
252 Neandertals is estimated to have occurred into the population ancestral to this ancient *Homo*
253 *sapiens*, 232-430 generations before his lifetime. His DNA carries segments of Neandertal
254 ancestry that are longer and more abundant than those in contemporary modern humans⁷¹. It is
255 thus tempting to interpret this result as a consequence of the hybridisation event. Besides similar
256 LD in the longer introgressed regions, a non-exclusive possibility is that the recombination
257 landscape of Ust'Ishim was influenced by trans-acting alleles inherited from Neandertals,
258 presumably acting at a larger scale than PRDM9. This could explain the discrepancy between
259 recombination-based trees at the large *versus* fine scale (where rapid evolution of PRDM9 would
260 quickly erode the signal of introgression), although further investigation is needed to test this
261 hypothesis – ideally, as the number of high-quality archaic genomes continues to increase in the
262 next years. Concretely, these results show that 1) iSMC can be used to extract information from
263 archaic genomes; 2) hotspot turn-over driven by PRDM9 not only is responsible for short time-
264 scale differences in the location of cross-over events, but the accumulation of such differences is

265 fast enough to have already impacted the landscape of *historical* recombination along the human
266 lineage; and 3) in hominids, the spatial distribution of cross-over events changes at a reasonably
267 constant rate, indicating that it evolves – to a large extent – neutrally.

268

269 **DISCUSSION:**

270 Our analyses have shown that iSMC is able to infer accurate recombination maps from single
271 pairs of genomes. Nevertheless, the correlations between statistical and experimental maps for
272 the three species are consistently lower than the correlations obtained during simulations. While
273 this difference can be partly explained by technical noise (e.g., sequencing or SNP calling
274 errors), there are alternative – and conceptually engaging – explanations for it. First, the different
275 types of data used by experimental and statistical methods imply that they measure different
276 facets of recombination. While experimental maps reflect the average cross-over rate (r) between
277 markers (i.e., a snapshot of the landscape at present-day generation), the population rate ρ
278 ($4.N_e.r$) estimated by iSMC depends on ancestral population sizes as well as on the variation of
279 N_e along the genome, and reflects the time-average of the historical recombination rate r . Since
280 regions of high r tend to erode quickly^{64,65}, the evolution of the recombination landscape over
281 time implies that ρ may be quite different from r (and more meaningful than r in the context of
282 population genomics⁵⁷). Second, biological processes that affect N_e locally (therefore distorting
283 the distribution of genealogies) but are unaccounted for by our model will affect LD without
284 reflecting the recombination rate. Among these, introgression and selective sweeps (through the
285 rapid increase of the frequency of advantageous haplotypes) can introduce a substantial bias if
286 prevalent along the genome. In a similar vein, background selection distorts the distribution of
287 genealogies towards lower TMRCA⁷², and should be common near regions under purifying
288 selection such as coding regions.

289

290 In order to study processes such as population structure⁶² and speciation^{57,73}, population

291 genomics generates high quality whole-genome sequences, with a small number of individuals
292 representing each of several sub-populations⁷³⁻⁷⁶. Due to the importance of linkage in ancestral
293 inference, recombination maps are key to analysing these data – and because of its power with
294 restricted sample sizes, iSMC is well suited for the task. We have demonstrated its accuracy in
295 species with contrasting levels of diversity, demographic histories and selective pressures, and
296 posit that it will be useful for investigation in other species. Not only will such maps aid the
297 interpretation of diversity in non-model organisms, but a picture of the recombination landscape
298 in different groups will tell us about the nature of recombination itself⁷⁷. Open questions include
299 whether the recombination landscape is associated with large-scale genome architecture and how
300 variation in the recombination landscape relates to life history and ecological traits. Finally, as
301 ancient DNA samples become more common (including species other than humans⁷⁸), it will be
302 possible to obtain maps from extinct *taxa*, granting the opportunity to study the evolution of the
303 recombination landscape with unprecedented resolution^{45,79}.

304

305 **METHODS:**

306 **The Markov-modulated Hidden Markov Model framework**

307 SMC models discretise a distribution of coalescence times into t intervals to implement a discrete
308 space Hidden Markov Model (HMM) with $t \times t$ transition matrix:

309

$$310 \quad \mathbf{Q}(\rho)_{smc} = \begin{bmatrix} G_{11} & G_{12} & \cdots & G_{1t} \\ G_{21} & & & G_{2t} \\ \vdots & & & \vdots \\ G_{t1} & G_{t2} & \cdots & G_{tt} \end{bmatrix}$$

311

312 where G_{ij} (the transition probabilities between genealogies i and j) is a function of ancestral
313 coalescence rates and the global parameter ρ , which is assumed to be constant along the
314 genome^{40,44}. The key innovation in iSMC is to relieve this assumption by letting ρ vary along the

315 genome, following its own Markov process, where values drawn from an a priori distribution are
 316 used to compute the transition probabilities between genealogies. Let R be any strictly positive
 317 probability distribution with mean = 1.0 describing the variation in recombination along the
 318 genome. If R is discretised into k categories of equal density, the possible values that ρ can
 319 assume in the Markov-modulated process are all $r_j * \rho_0$, where r_j is the j th R category and ρ_0 is the
 320 genome-wide average recombination rate. Our Markov model (inspired by the observation that
 321 the distribution of cross-over events is not random, but clustered in regions of similar values)
 322 states that the probability distribution of R at position $x + 1$ only depends on the the distribution
 323 at position x . We consider the case where the transition probability between any two R categories
 324 (P_{ij}) is identical and equivalent to one auto-correlation parameter (δ). The transition matrix of
 325 this Markovian process is simply:

326

$$327 \quad \mathbf{Q}_\rho = \begin{bmatrix} P_{11} & P_{12} & \dots & P_{1k} \\ P_{21} & & & P_{2k} \\ \vdots & & & \vdots \\ P_{k1} & P_{k2} & \dots & P_{kk} \end{bmatrix} = \begin{bmatrix} 1-\delta & \frac{\delta}{k-1} & \dots & \frac{\delta}{k-1} \\ \frac{\delta}{k-1} & 1-\delta & & \frac{\delta}{k-1} \\ \vdots & & & \vdots \\ \frac{\delta}{k-1} & \frac{\delta}{k-1} & \dots & 1-\delta \end{bmatrix}$$

328

329 Because ρ is a parameter of the SMC, variation in the recombination rate affects the transition
 330 probabilities between genealogies (\mathbf{Q}_{SMC}). Since spatial variation in ρ is modeled as a Markovian
 331 process, the combined process is said to be Markov-modulated by ρ , leading to a Markov-
 332 modulated HMM. If t is the number of discrete genealogies of the SMC, and k is the number of
 333 discretised ρ categories, then the Markov-modulated HMM is a HMM with $n = t \times k$ hidden
 334 states (**Figure 1**). We further disallow transitions between hidden states where both the
 335 genealogies and ρ values change simultaneously. In this case, the transition matrix of the
 336 Markov-modulated process, \mathbf{Q}_{ISMC} , is given by:

337

338
$$\text{diag}(Q_p) \otimes Q_{SMC} + (Q_p - \text{diag}(Q_p)) \otimes I_t$$

339

340 where \hat{u} denotes the Kronecker product and I_t the identity matrix of dimension t . Since many of

341 its elements are reduced to zero, the matrix can be transversed efficiently:

342

343
$$Q_{iSMC} = \begin{bmatrix} P_{11} \cdot Q(\rho_1)_{SMC} & P_{12} \cdot I_t & \cdots & P_{1k} \cdot I_t \\ P_{21} \cdot I_t & P_{22} \cdot Q(\rho_{22})_{SMC} & & P_{2k} \cdot I_t \\ \vdots & & & \vdots \\ P_{k1} \cdot I_t & P_{k2} \cdot I_t & \cdots & P_{kk} \cdot Q(\rho_k)_{SMC} \end{bmatrix}$$

344

345 In other words, Q_{iSMC} is a composition of k^2 square sub-matrices of dimension t . The main

346 diagonal sub-matrices are Q_{SMC} assembled using the corresponding ρ value for category k (and

347 scaled by $1 - \delta$), while the off-diagonal sub-matrices are identity matrices which have δ as main

348 diagonal elements.

349

350 **Modelling spatial variation in recombination rates**

351 iSMC implements three models of spatial variation in the recombination rate. We first use a

352 Gamma probability density function with a single parameter ($\alpha = \text{beta}$), which constrains it to

353 have a mean equal to 1.0. After discretisation into k categories of equal density, the mean value

354 inside each category is drawn to scale the genome-wide average ρ during integration over all

355 recombination rates in the forward recursion (**equation 1**). In our simulation study, since we

356 used a continuous Gamma distribution to draw values of the recombination landscape, we used

357 this model to infer recombination maps. In the second model, we extend the gamma distribution

358 by adding a category that represents the intensity of the recombination rate in sharp hotspots

359 (parameter H). Since hotspots are narrow relative to the extension of the background

360 recombination rate, we use extra parameters to accommodate this effect. As before, δ is the

361 transition probability between gamma categories, and we introduce u as the transition probability

362 from any gamma category to H , and v as the transition probability from H to any gamma
363 category. The third model is obtained by letting the number of discretised categories of the
364 Gamma distribution equal to 1, such that it becomes a probability mass function of two
365 categories (**Supplemental Note**).

366

367 **Model selection and computation of the posterior recombination landscape**

368 iSMC works in two steps: (1) fitting models of recombination rate variation and (2) inferring
369 recombination maps based on the selected model. During step 1, the model parameters are
370 optimized by maximizing the likelihood using the Powell multi-dimensions procedure⁸⁰, which is
371 computed for the entire sequence by applying the forward recursion of the HMM⁴⁸ at every
372 position x of the alignment:

373

374 **equation 1**
$$F_{S_x, G_u}(\rho_l) = \left(\sum_k \left(\sum_t F_{S_{(x-1)}, G_t}(\rho_k) \cdot Pr(G_t \rightarrow G_u | \rho_k) \cdot Pr(\rho_k \rightarrow \rho_l) \right) \right) \cdot Pr(G_u \rightarrow S_x)$$

375

376 where we integrate over all k discretized values of ρ and over all t TMRCA intervals. The
377 transition between genealogies ($G_t \rightarrow G_u$) is a function of both the focal recombination rate
378 (ρ_k) and the ancestral coalescence rates, and $G_u \rightarrow S_x$ represents the emission probability from
379 G_u to the observed binary state at position x (**Supplemental Note**). In case AIC favours one of
380 the heterogeneous models, in step 2 iSMC uses the estimated parameters to estimate the posterior
381 average ρ for all sites in the genome. To this end, it first uses the so-called posterior decoding
382 method⁴⁸ as implemented in zipHMMLib⁸¹ to compute the posterior probability of every hidden
383 state at each position in the sequence. Since in the Markov-modulated HMM the hidden states
384 are pairs of ρ categories and TMRCA intervals, this results in joint probability distributions of
385 recombination values and coalescence times, for all sites in the genome. Thus, prior to
386 computing the posterior average, iSMC obtains the marginal distribution over recombination
387 rates: if ${}^n\mathbf{Y}_x$ is the n -dimensional vector containing posterior probabilities for all n hidden states

388 at position x , where n is the product of t TMRCA intervals and k ρ categories, iSMC obtains the
389 k -dimensional vector ${}^k\mathbf{Z}_x$ by summing, for all k , the posterior probabilities of every hidden state n
390 matching ρ category k . Finally, iSMC uses ${}^k\mathbf{Z}_x$ to scale the corresponding values of the discretized
391 distribution of ρ , such that the posterior average ρ for position x is $(\overline{\rho}_x) = \sum_k {}^kZ_x \cdot \rho_k$.

392

393 **Modelling complex demographic histories**

394 The original HMM implementation of the SMC⁴³ uses the expectation-maximisation algorithm to
395 optimise transition probabilities, where the actual targets of inference – the coalescence rates at
396 each time interval – are hyper-parameters of the model. Here we use cubic spline interpolation⁴²
397 to map coalescence rates at time boundaries, which are then assumed to be piecewise constant
398 for the duration of each interval. Because we use three internal splines knots (i.e., the
399 demographic history is divided into four epochs wherein a cubic curve is fitted), the number of
400 parameters is substantially reduced in our model – in particular when a fine discretisation of
401 TMRCA is employed.

402

403 **Simulation study**

404 *Four scenarios of spatial variation in ρ .* We simulated a piecewise constant recombination rate
405 along the genome by drawing values from a gamma distribution with parameters α and β , and
406 segment lengths from a geometric distribution with mean length g . We considered four possible
407 scenarios where $\alpha = \beta = 0.5$ or 5.0 , and $g = 100$ kb or 1 Mb. For each of the four combinations,
408 we simulated 10 independent pairs of two 30 Mb haploid chromosomes under a constant
409 population size model, assuming $\theta = 0.003$ and $\rho = 0.0012$. For each of the following simulated
410 scenarios, we focus on the landscape with $\alpha = 0.5$ and $g = 100$ kb. All scenarios share base
411 parameters values (θ , ρ , sequence length and sample size).

412

413 *Demographic history.* We simulated two demographic scenarios. First, a 20-fold population

414 expansion 0.01 coalescent time units ago; second, a 20-fold population bottleneck 0.5 coalescent
415 time units ago. Translating these coalescent times based on effective population sizes, the
416 expansion happened 600 generations ago, and the bottleneck happened 30,000 generations ago.

417

418 *Introgression events.* We simulated two introgression scenarios where a source population
419 introduces a pulse of genetic material into a target population. In both scenarios, the split
420 between source and target populations happened 2.0 coalescent time units ago, and the source
421 replaces 10% of the genetic pool of the target. In the first scenario, secondary contact happened
422 0.125 coalescent time units ago; in the second, it happened 0.25 coalescent time units ago.
423 Translating these coalescent times based on effective population sizes, the split between
424 population happened 120,000 generations ago, and the introgression events happened 7,500 and
425 15,000 generations ago, respectively.

426

427 *Variation in the mutation rate.* We simulated a piecewise constant mutation rate along the
428 genome by drawing rate values from a uniform distribution and segment lengths from a
429 geometric distribution with mean length f , where f is either 20 kb or 500 kb. The uniform
430 distribution generating scaling factors of θ has mean = 5.05 instead of 1.0. In this case, the
431 expected genome-wide average $\theta = 0.015$. The reason for that is our focus on the spatial
432 distribution of θ itself. If the landscape had mean = 0.003, its highly heterogeneous nature would
433 scale θ down to values well below ρ (0.0012) too often along the 30 Mb sequence. The ensuing
434 loss of signal (due to low SNP density) would result in poorly inferred maps that display low
435 correlations with the simulations, not because of spatial *heterogeneity* in θ (local transitions), but
436 instead because the ratio θ / ρ would be too low in many windows across the chromosome.

437

438 **Code availability**

439 Source code for iSMC, as well as executable files with an example dataset, can be obtained at

440 [github repository will be made public upon publication]. R scripts used both for simulations and
441 data analyses are available in **Supplemental Data 1**.

442

443 **Data analysis**

444 Model selection followed by inference of recombination maps in the three species studied (**Table**
445 **1**) was performed using publicly available sequences (chromosome 2L from haploid pairs
446 ZI161 / ZI170, ZI179 / ZI191 and ZI129 / ZI138 in the *Drosophila* Population Genomics Project
447 Phase 3⁸²; chromosome 1 from haploid pairs Zt09 / Zt150, Zt154 / Zt155 and Zt05 / Zt07 for
448 *Zymoseptoria tritici*³¹; chromosome 10 from three Finnish individuals (LP6005442-DNA_C10,
449 LP6005442-DNA_D10, LP6005592-DNA_A02) available in the Simons Genome Diversity
450 Project⁶² for humans). In the first two species, gaps and unknown nucleotides in the sequences
451 (in FASTA format) were assigned as missing data, whereas in Humans the available strict mask
452 for the dataset was applied after parsing the VCF files.

453

454 iSMC was fitted four times to each pair of genomes of the three species: 1) with 40 discretised
455 time intervals and a model of variation in ρ based on a Gamma distribution with five discretised
456 categories; 2) with 40 discretised time intervals and a model of variation in ρ based on an
457 extended Gamma distribution with four discretised categories and an additional “Hotspot”
458 category; 3) with 40 discretised time intervals and a model of variation in ρ based on a
459 probability mass function of two categories; 4) with 100 discretised time intervals and a model of
460 variation in ρ based on a probability mass function of two categories. In each case, Kendall
461 correlation of ranks was computed between the resulting recombination landscape and available
462 genetic maps both at the fine scale (100 kb for *Drosophila*, 20 kb for *Zymoseptoria tritici* and 50
463 kb for Humans) and at the large scale (1 Mb for *Drosophila*, 200 kb for *Zymoseptoria tritici* and 1
464 Mb for Humans).

465

466 Whole-genome sequence data were used for in-depth analyses of the recombination landscape in
467 the hominid clade. Model fit (based on the “Hotspot” distribution) and inference of
468 recombination maps was performed independently on each chromosome. The individual IDs
469 within the Simons Genome Diversity Project⁶² and corresponding population of origin of the nine
470 contemporary modern humans are as follows: African (Yoruban): LP6005442-DNA_A02,
471 LP6005442-DNA_B02 and SS6004475; Asian (Dai Chinese): LP6005441-DNA_D04,
472 LP6005443-DNA_B01 and LP6005592-DNA_D03; European (Finnish): LP6005442-
473 DNA_C10, LP6005442-DNA_D10, LP6005592-DNA_A02. The available strict mask for the
474 dataset was applied to assign low-quality positions as missing data. The four ancient DNA
475 samples were downloaded from the server at the Max Planck Institute for Evolutionary
476 Anthropology in Leipzig (<http://cdna.eva.mpg.de/neandertal/Vindija/VCF/>) in May 2018. Since
477 these are complete VCF files where all callable positions are reported, no mask was used and
478 absent positions were assigned as missing data.

479

480 The analyses of modern and archaic datasets was performed considering only positions present
481 in the DECODE genetic map. The dendrogram presented in **Figure 4** was obtained by
482 hierarchical clustering (using complete linkage) of pair-wise distances computed from $1 - \tau$,
483 where τ is the Kendall correlation of ranks between two individual recombination maps.

484 Recombination maps for the entire archaic sequences are available as a resource in

485 **Supplemental Data 2.**

486

487 **Acknowledgements**

488 The authors thank Alice Feurtey, Asger Hobolth, Bernhard Haubold, Eva Stukenbrock, Fabian
489 Klötzl, Kai Zeng, Pier Palamara and Stephan Schiffels for fruitful discussions about this work.
490 JYD acknowledges funding from the Max Planck Society. This work was supported by a grant
491 from the German Research Foundation (Deutsche Forschungsgemeinschaft) attributed to JYD,

492 within the priority program (SPP) 1590 “probabilistic structures in evolution”.

493

494 **Author Contributions**

495 JYD and GVB conceived and designed the study, analysed the datasets and wrote the

496 manuscript. GVB developed the software. GVB and NP performed the simulation study.

497

498 The authors declare that there are no conflict of interest regarding the publication of this article.

499

500 **Table 1: Performance of iSMC in three distantly related species. AIC and Kendall**
 501 correlations between individual recombination maps and a genetic map from each species.

		Drosophila (chr 2L) 100-kb / 1-Mb			Zymoseptoria (chr 1) 20-kb / 200-kb			Humans (chr 10) 50-kb / 1-Mb		
Configuration		Sample 1	Sample 2	Sample 3	Sample 1	Sample 2	Sample 3	Sample 1	Sample 2	Sample 3
AIC	40x5	2240174.6	2247931.8	2207295.4	572264.6	589366.4	589410.5	1399031.9	1374656.2	1434109.5
	40x(4+1)	2240269.1	2247937.7	2207417.0	572101.7	589772.2	589614.0	1399099.2	1374692.4	1434148.8
	40x2	2240267.8	2248028.2	2207415.9	571974.0	589392.2	589509.4	1399096.3	1374690.3	1434146.9
	100x2	2240359.0	2247948.0	2207537.0	571756.1	588792.1	588748.8	1398867.6	1374403.8	1433950.9
Cor. fine-scale	40x5	0.363***	0.334***	0.342***	0.041	0.118**	0.245***	0.189***	0.196***	0.192***
	40x(4+1)	0.294***	0.267***	0.300***	0.216***	0.272***	0.282***	0.196***	0.191***	0.179***
	40x2	0.293***	0.261***	0.300	0.217***	0.225***	0.223***	0.198***	0.192***	0.180***
	100x2	0.289***	0.265***	0.298***	0.287***	0.279***	0.308***	0.211***	0.190***	0.179***
Cor. large-scale	40x5	0.613***	0.549***	0.644***	-0.306*	-0.007	0.191	0.445***	0.436***	0.460***
	40x(4+1)	0.502***	0.455**	0.494***	0.421***	0.471***	0.499***	0.449***	0.445***	0.452***
	40x2	0.510***	0.423**	0.494***	0.398**	0.476***	0.421***	0.448***	0.449***	0.450***
	100x2	0.494***	0.439**	0.486***	0.499***	0.393**	0.476***	0.455***	0.445***	0.446***

502

503 * p-value < 0.05; ** p-value < 0.01; *** p-value < 0.001

504

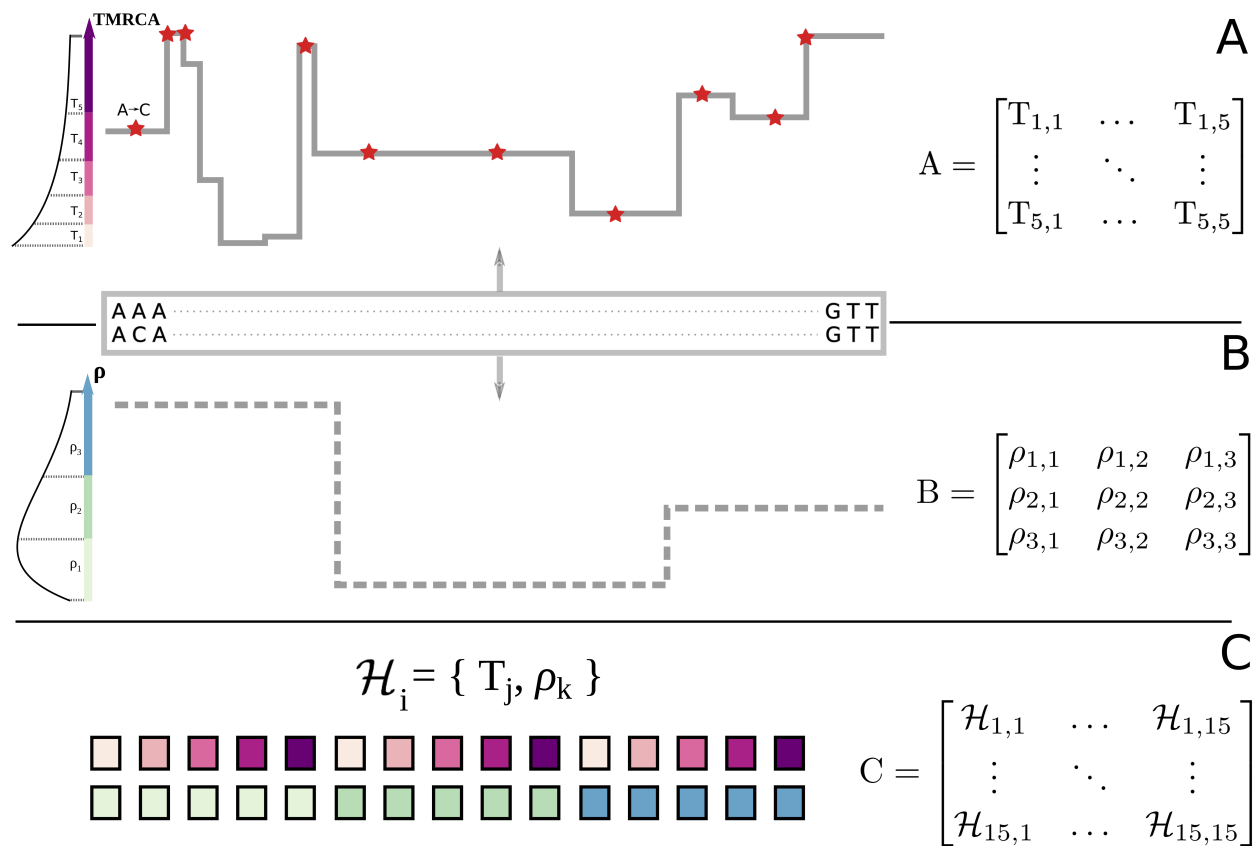
505 **Table 2: Performance of iSMC in distinct human populations.** Kendall correlations between
506 individually inferred recombination maps for each of three human populations and the DECODE
507 genetic map. All values are significant with p-value < 0.001.

	Bin Size	Sample 1	Sample 2	Sample 3	Consensus
	50kb	0.116	0.154	0.148	0.177
African (Yoruba)	200kb	0.171	0.236	0.219	0.267
	500kb	0.235	0.309	0.271	0.319
	1mb	0.309	0.388	0.338	0.431
	50kb	0.185	0.177	0.191	0.251
Asian (Dai Chinese)	200kb	0.312	0.273	0.261	0.348
	500kb	0.397	0.406	0.369	0.464
	1mb	0.473	0.457	0.436	0.508
	50kb	0.211	0.190	0.179	0.253
508 European (Finnish)	200kb	0.277	0.295	0.283	0.356
	500kb	0.397	0.366	0.363	0.447
	1mb	0.455	0.445	0.446	0.521

509

510 FIGURES

511 **Figure 1. Schematic representation of iSMC for one pair of genomes, with five time**
 512 **intervals and three recombination rate categories. A,** In the SMC process, the spatial
 513 distribution of TMRCA can be described by a matrix of transition probabilities that depend on
 514 local population recombination rate ρ and the ancestral coalescence rates. **B,** variation in ρ along
 515 the genome, modelled as a Markovian process and described by a matrix of transition
 516 probabilities. **C,** the combination of both Markovian processes leads to a Markov-modulated
 517 Markovian process. The hidden states of the resulting hidden Markov model are all pairwise
 518 combinations of discretized classes in **A** and **B**.
 519



521

522

523

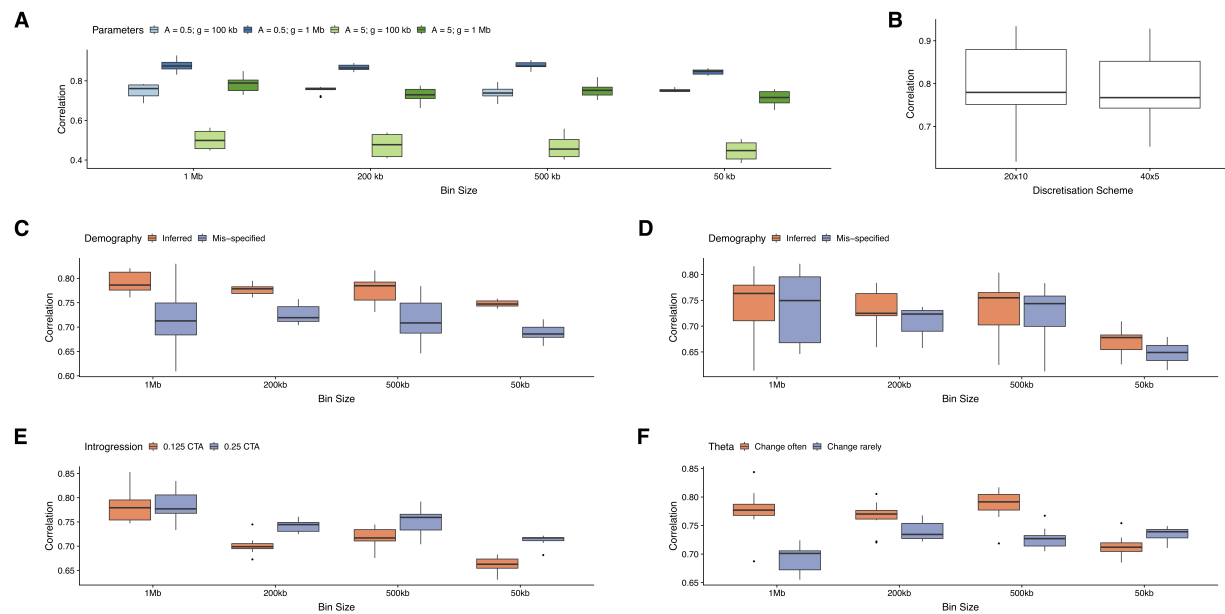
524

525

526

527

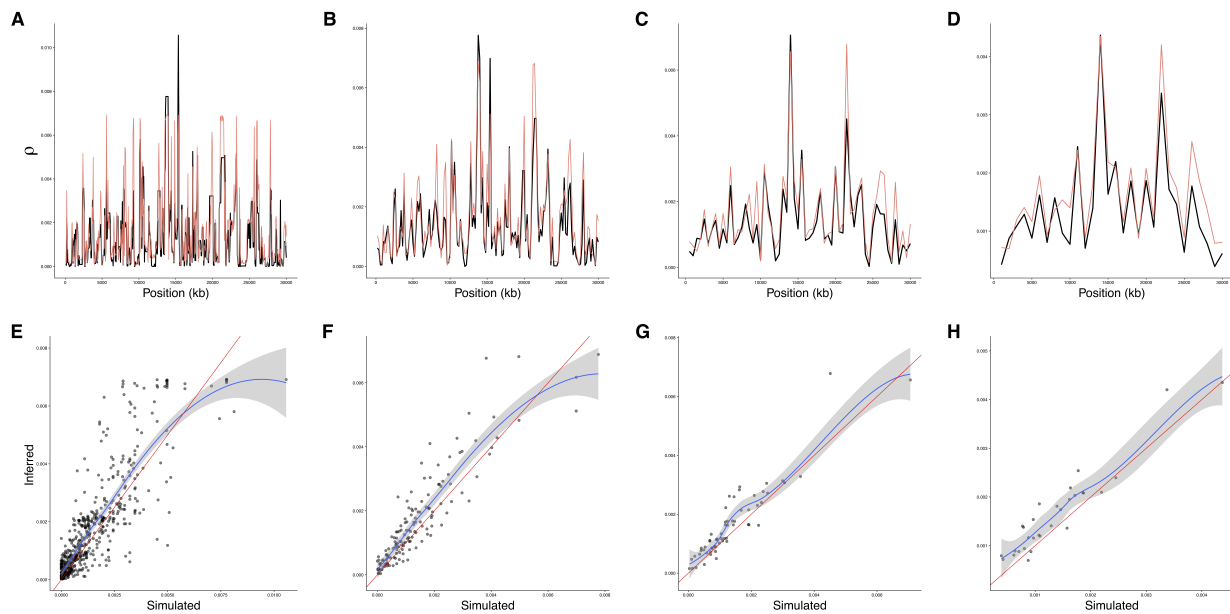
528 **Figure 2. Distribution of correlation coefficients in the simulation study.** Center line,
529 median; box limits, upper and lower quartiles; whiskers, 1.5x interquartile range; points, outliers.
530 **A**, four scenarios of spatial variation in the recombination rate, corresponding to different
531 combinations of parameters (colour). **B**, the respective comparison between two discretisation
532 schemes in the four recombination landscapes. **C-D**, comparison between a model where
533 demography is mis-specified and another where it is jointly inferred (colour), in scenarios of
534 recent growth (**C**) or ancient bottleneck (**D**). **E**, two scenarios of introgression, varying the time
535 of gene-flow (colour). **F**, two scenarios of spatial variation in the mutation rate, varying its
536 frequency of change (colour).
537



539
540
541
542
543
544
545
546
547
548
549
550

551 **Figure 3. Inference of recombination maps in the presence of recent population growth.**

552 Each column represents a bin size (50 kb, 200 kb, 500 kb and 1 Mb). **A-D**, Simulated (black) and
553 inferred (orange) recombination maps. **E-H**, scatter-plots of the same data. Red lines represent y
554 $= x$, blue lines represent loess smoothing curve.



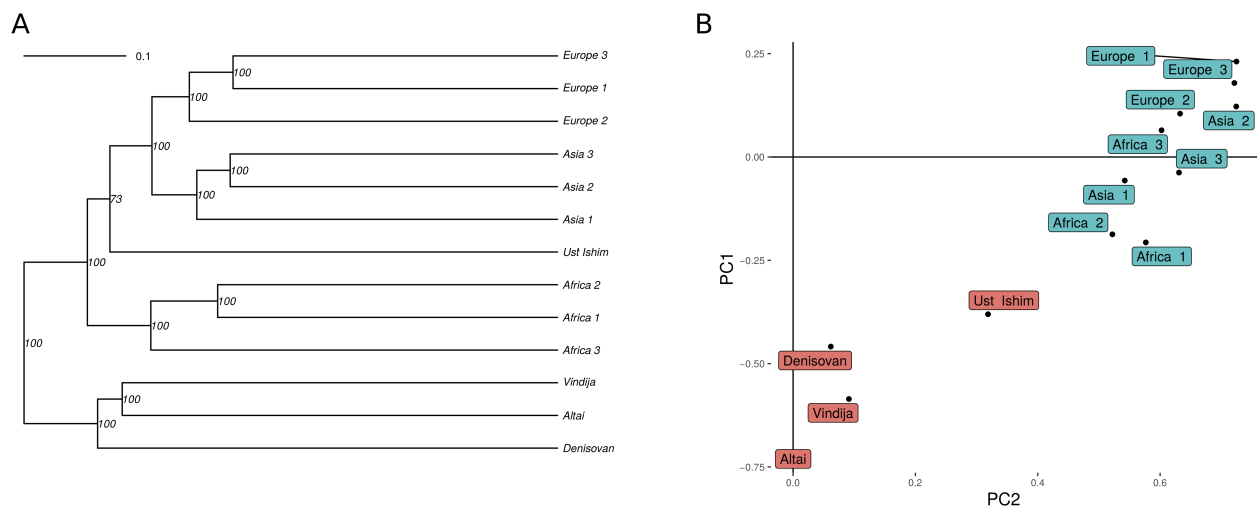
556

557

558 **Figure 4. Evolution of the fine-scale recombination landscape in hominids.** **A**, Dendrogram

559 based on pair-wise correlations between whole-genome recombination maps at the 50 kb scale. **B**,

560 principal component analysis of the same data.



562

563

564

565 SUPPLEMENTAL FIGURE LEGENDS

566 **Figure S1. Inference of recombination maps in the presence of a heterogeneous mutation**
567 **landscape.** Points are coloured as a function of the local ratio θ / ρ (≥ 1 green, < 1 pink).
568 Magenta dashed line represents $y = x$. **A**, both ρ and θ are binned into 50 kb windows. Solid lines
569 represent loess smoothing curves fitted to each class of θ / ρ , with 95% confidence intervals
570 around them (shaded). **B**, both ρ and θ were binned into 500 kb windows.
571

572 **Figure S2. Evolution of the large-scale recombination landscape in hominids. A-C,**
573 Dendrogram based on pair-wise correlations between whole-genome recombination maps at the
574 50 kb, 200 kb and 1 Mb scales. **D-F**, principal component analysis of the same data.
575

576 REFERENCES

1. Keightley, P. D. & Otto, S. P. Interference among deleterious mutations favours sex and recombination in finite populations. *Nature* **443**, 89–92 (2006).
2. Hill, W. G. & Robertson, A. The effect of linkage on limits to artificial selection. *Genet. Res.* **8**, 269–294 (1966).
3. Smith, J. M. & Haigh, J. The hitch-hiking effect of a favourable gene. *Genet. Res.* **89**, 391–403 (2007).
4. Ellegren, H. & Galtier, N. Determinants of genetic diversity. *Nat. Rev. Genet.* **17**, 422–433 (2016).
5. Boulton, a, Myers, R. S. & Redfield, R. J. The hotspot conversion paradox and the evolution of meiotic recombination. *Proceedings of the National Academy of Sciences of the United States of America* **94**, 8058–8063 (1997).
6. Myers, S. *et al.* Drive against hotspot motifs in primates implicates the PRDM9 gene in meiotic recombination. *Science* **327**, 876–879 (2010).
7. Kong, A. *et al.* Fine-scale recombination rate differences between sexes, populations and individuals. *Nature* **467**, 1099–1103 (2010).
8. Kawakami, T. *et al.* Whole-genome patterns of linkage disequilibrium across flycatcher populations clarify the causes and consequences of fine-scale recombination rate variation in birds. *Mol. Ecol.* **26**, 4158–4172 (2017).

9. Dumont, B. L. & Payseur, B. A. Genetic Analysis of Genome-Scale Recombination Rate Evolution in House Mice. *PLOS Genetics* **7**, e1002116 (2011).
10. Baudat, F. *et al.* PRDM9 is a major determinant of meiotic recombination hotspots in humans and mice. *Science* **327**, 836–840 (2010).
11. Auton, A. *et al.* A fine-scale chimpanzee genetic map from population sequencing. *Science* **336**, 193–198 (2012).
12. Singhal, S. *et al.* Stable recombination hotspots in birds. *Science* **350**, 928–932 (2015).
13. Heil, S., S. C., Ellison, C., Dubin, M. & Noor, M. A. F. Recombining without Hotspots: A Comprehensive Evolutionary Portrait of Recombination in Two Closely Related Species of *Drosophila*. *Genome Biol Evol* **7**, 2829–2842 (2015).
14. Brand, C. L., Cattani, M. V., Kingan, S. B., Landeen, E. L. & Presgraves, D. C. Molecular Evolution at a Meiosis Gene Mediates Species Differences in the Rate and Patterning of Recombination. *Current Biology* **28**, 1289–1295.e4 (2018).
15. Kohl, K. P., Jones, C. D. & Sekelsky, J. Evolution of an MCM complex in flies that promotes meiotic crossovers by blocking BLM helicase. *Science* **338**, 1363–1365 (2012).
16. Cutter, A. D. & Payseur, B. A. Genomic signatures of selection at linked sites: unifying the disparity among species. *Nature reviews. Genetics* **14**, 262–74 (2013).
17. Wang, J., Street, N. R., Scofield, D. G. & Ingvarsson, P. K. Natural Selection and Recombination Rate Variation Shape Nucleotide Polymorphism Across the Genomes of Three Related *Populus* Species. *Genetics* **202**, 1185–1200 (2016).
18. Schumer, M. *et al.* Natural selection interacts with recombination to shape the evolution of hybrid genomes. *Science* eaar3684 (2018). doi:10.1126/science.aar3684
19. Murray, G. G. R. *et al.* Natural selection shaped the rise and fall of passenger pigeon genomic diversity. *Science* **358**, 951–954 (2017).
20. Martin, S. H. & Jiggins, C. D. Interpreting the genomic landscape of introgression. *Curr. Opin. Genet. Dev.* **47**, 69–74 (2017).
21. Visscher, P. M. *et al.* 10 Years of GWAS Discovery: Biology, Function, and Translation. *The American Journal of Human Genetics* **101**, 5–22 (2017).
22. Duret, L. & Galtier, N. Biased gene conversion and the evolution of mammalian genomic landscapes. *Annu Rev Genomics Hum Genet* **10**, 285–311 (2009).

23. Kostka, D., Hubisz, M. J., Siepel, A. & Pollard, K. S. The Role of GC-Biased Gene Conversion in Shaping the Fastest Evolving Regions of the Human Genome. *Mol Biol Evol* **29**, 1047–1057 (2012).
24. Bolívar, P., Mugal, C. F., Nater, A. & Ellegren, H. Recombination Rate Variation Modulates Gene Sequence Evolution Mainly via GC-Biased Gene Conversion, Not Hill–Robertson Interference, in an Avian System. *Molecular Biology and Evolution* **33**, 216–227 (2016).
25. Glémin, S. *et al.* Quantification of GC-biased gene conversion in the human genome. *Genome Res.* **25**, 1215–1228 (2015).
26. Stumpf, M. P. H. & McVean, G. a. T. Estimating recombination rates from population-genetic data. *Nature Reviews Genetics* **4**, 959–968 (2003).
27. Rosenberg, N. A. & Nordborg, M. Genealogical Trees, Coalescent Theory and the Analysis of Genetic Polymorphisms. *Nature Reviews Genetics* **3**, 380–390 (2002).
28. McVean, G. A. T. *et al.* The fine-scale structure of recombination rate variation in the human genome. *Science* **304**, 581–584 (2004).
29. Auton, A. & McVean, G. Recombination rate estimation in the presence of hotspots. *Genome Res* **17**, 1219–1227 (2007).
30. Chan, A. H., Jenkins, P. A. & Song, Y. S. Genome-Wide Fine-Scale Recombination Rate Variation in *Drosophila melanogaster*. *PLOS Genetics* **8**, e1003090 (2012).
31. Stukenbrock, E. H. & Dutheil, J. Y. Fine-Scale Recombination Maps of Fungal Plant Pathogens Reveal Dynamic Recombination Landscapes and Intragenic Hotspots. *Genetics* **208**, 1209–1229 (2018).
32. Hudson, R. R. Two-Locus Sampling Distributions and Their Application. *Genetics* **159**, 1805–1817 (2001).
33. Hudson, R. R. & Kaplan, N. L. Statistical properties of the number of recombination events in the history of a sample of DNA sequences. *Genetics* **111**, 147–164 (1985).
34. Hudson, R. R. & Kaplan, N. L. The coalescent process in models with selection and recombination. *Genetics* **120**, 831–840 (1988).
35. Wiuf, C. & Hein, J. Recombination as a point process along sequences. *Theoretical population biology* **55**, 248–59 (1999).
36. Griffiths, R. C. & Marjoram, P. An ancestral recombination graph. in *Progress in population*

- genetics and human evolution* 257–270 (Springer, 1997).
37. Griffiths, R. C. & Marjoram, P. Ancestral inference from samples of DNA sequences with recombination. *J. Comput. Biol.* **3**, 479–502 (1996).
 38. Hein, J., Schierup, M. & Wiuf, C. *Gene Genealogies, Variation and Evolution: A primer in coalescent theory*. (Oxford University Press, 2004).
 39. McVean, G. A. T. & Cardin, N. J. Approximating the coalescent with recombination. *Philosophical Transactions of the Royal Society B: Biological Sciences* **360**, 1387–1393 (2005).
 40. Marjoram, P. & Wall, J. D. Fast ‘coalescent’ simulation. *BMC Genetics* **7**, 16–16 (2006).
 41. Wilton, P. R., Carmi, S. & Hobolth, A. The SMC Is a Highly Accurate Approximation to the Ancestral Recombination Graph. *Genetics* **200**, 343–355 (2015).
 42. Terhorst, J., Kamm, J. A. & Song, Y. S. Robust and scalable inference of population history from hundreds of unphased whole-genomes. *Nat Genet* **49**, 303–309 (2017).
 43. Li, H. & Durbin, R. Inference of human population history from individual whole-genome sequences. *Nature* **475**, 493–496 (2011).
 44. Schiffels, S. & Durbin, R. Inferring human population size and separation history from multiple genome sequences. *Nature Genetics* **46**, 919–925 (2014).
 45. Munch, K., Schierup, M. H. & Mailund, T. Unraveling recombination rate evolution using ancestral recombination maps. *Bioessays* **36**, 892–900 (2014).
 46. Munch, K., Mailund, T., Dutheil, J. Y. & Schierup, M. H. A fine-scale recombination map of the human-chimpanzee ancestor reveals faster change in humans than in chimpanzees and a strong impact of GC-biased gene conversion. *Genome Res.* **24**, 467–474 (2014).
 47. Dutheil, J. Y. Hidden Markov Models in Population Genomics. *Methods Mol. Biol.* **1552**, 149–164 (2017).
 48. Durbin, R., Eddy, S. R., Krogh, A. & Mitchison, G. *Biological sequence analysis: Probabilistic models of proteins and nucleic acids*. (Cambridge University Press, 1998). doi:10.1017/CBO9780511790492
 49. Slatkin, M. Linkage disequilibrium--understanding the evolutionary past and mapping the medical future. *Nature reviews. Genetics* **9**, 477–85 (2008).
 50. McVean, G. A. T. A genealogical interpretation of linkage disequilibrium. *Genetics* **162**,

- 987–991 (2002).
51. Wirtz, J., Rauscher, M. & Wiehe, T. Topological linkage disequilibrium calculated from coalescent genealogies. *Theoretical Population Biology* (2018).
doi:10.1016/j.tpb.2018.09.001
 52. Akaike, H. A new look at the statistical model identification. *IEEE Transactions on Automatic Control* **19**, 716–723 (1974).
 53. Staab, P. R., Zhu, S., Metzler, D. & Lunter, G. Scrm: Efficiently simulating long sequences using the approximated coalescent with recombination. *Bioinformatics* **31**, 1680–1682 (2015).
 54. Dapper, A. L. & Payseur, B. A. Effects of Demographic History on the Detection of Recombination Hotspots from Linkage Disequilibrium. *Mol. Biol. Evol.* **35**, 335–353 (2018).
 55. Johnston, H. R. & Cutler, D. J. Population demographic history can cause the appearance of recombination hotspots. *Am. J. Hum. Genet.* **90**, 774–783 (2012).
 56. Kamm, J. A., Spence, J. P., Chan, J. & Song, Y. S. Two-Locus Likelihoods Under Variable Population Size and Fine-Scale Recombination Rate Estimation. *Genetics* **203**, 1381–1399 (2016).
 57. Martin, S. H., Davey, J., Salazar, C. & Jiggins, C. Recombination rate variation shapes barriers to introgression across butterfly genomes. *bioRxiv* 297531 (2018).
doi:10.1101/297531
 58. Grossen, C., Keller, L., Biebach, I., Consortium, T. I. G. G. & Croll, D. Introgression from Domestic Goat Generated Variation at the Major Histocompatibility Complex of Alpine Ibex. *PLOS Genetics* **10**, e1004438 (2014).
 59. Francioli, L. C. *et al.* Genome-wide patterns and properties of *de novo* mutations in humans. *Nature Genetics* **47**, 822–826 (2015).
 60. Hartmann, F. E., McDonald, B. A. & Croll, D. Genome-wide evidence for divergent selection between populations of a major agricultural pathogen. *Molecular Ecology* **27**, 2725–2741
 61. Croll, D., Lendenmann, M. H., Stewart, E. & McDonald, B. A. The impact of recombination hotspots on genome evolution of a fungal plant pathogen. *Genetics* **201**, 1213–1228 (2015).
 62. Mallick, S. *et al.* The Simons Genome Diversity Project: 300 genomes from 142 diverse

- populations. *Nature* (2016). doi:10.1038/nature18964
63. Paigen, K. & Petkov, P. M. PRDM9 and Its Role in Genetic Recombination. *Trends Genet.* **34**, 291–300 (2018).
 64. Coop, G. & Myers, S. R. Live hot, die young: Transmission distortion in recombination hotspots. *PLoS Genetics* **3**, 0377–0386 (2007).
 65. Lattille, T., Duret, L. & Lartillot, N. The Red Queen model of recombination hot-spot evolution: a theoretical investigation. *Phil. Trans. R. Soc. B* **372**, 20160463 (2017).
 66. Lesecque, Y., Glémin, S., Lartillot, N., Mouchiroud, D. & Duret, L. The Red Queen Model of Recombination Hotspots Evolution in the Light of Archaic and Modern Human Genomes. *PLOS Genetics* **10**, e1004790 (2014).
 67. Slatkin, M. & Racimo, F. Ancient DNA and human history. *PNAS* **113**, 6380–6387 (2016).
 68. Prüfer, K. *et al.* The complete genome sequence of a Neanderthal from the Altai Mountains. *Nature* **505**, 43–49 (2013).
 69. Green, R. E. *et al.* A draft sequence of the Neandertal genome. *Science (New York, N.Y.)* **328**, 710–22 (2010).
 70. Meyer, M. *et al.* A High-Coverage Genome Sequence from an Archaic Denisovan Individual. *Science* **338**, 222–226 (2012).
 71. Fu, Q. *et al.* Genome sequence of a 45,000-year-old modern human from western Siberia. *Nature* **514**, 445–449 (2014).
 72. Palamara, P. F., Terhorst, J., Song, Y. S. & Price, A. L. High-throughput inference of pairwise coalescence times identifies signals of selection and enriched disease heritability. *Nature Genetics* **50**, 1311–1317 (2018).
 73. Brandvain, Y., Kenney, A. M., Flagel, L., Coop, G. & Sweigart, A. L. Speciation and Introgression between *Mimulus nasutus* and *Mimulus guttatus*. *PLOS Genetics* **10**, e1004410 (2014).
 74. Teng, H. *et al.* Population Genomics Reveals Speciation and Introgression between Brown Norway Rats and Their Sibling Species. *Mol Biol Evol* **34**, 2214–2228 (2017).
 75. Van Belleghem, S. M. *et al.* Patterns of Z chromosome divergence among *Heliconius* species highlight the importance of historical demography. *Mol. Ecol.* (2018).
doi:10.1111/mec.14560

76. Delmore, K. E. *et al.* Comparative analysis examining patterns of genomic differentiation across multiple episodes of population divergence in birds. *Evolution Letters* **2**, 76–87 (2018).
77. Stapley, J., Feulner, P. G. D., Johnston, S. E., Santure, A. W. & Smadja, C. M. Variation in recombination frequency and distribution across eukaryotes: patterns and processes. *Phil. Trans. R. Soc. B* **372**, 20160455 (2017).
78. Librado, P. *et al.* Ancient genomic changes associated with domestication of the horse. *Science* **356**, 442–445 (2017).
79. Moorjani, P. *et al.* A genetic method for dating ancient genomes provides a direct estimate of human generation interval in the last 45,000 years. *PNAS* **113**, 5652–5657 (2016).
80. Guéguen, L. *et al.* Bio++: efficient extensible libraries and tools for computational molecular evolution. *Mol. Biol. Evol.* **30**, 1745–1750 (2013).
81. Sand, A., Kristiansen, M., Pedersen, C. N. & Mailund, T. zipHMMLib: a highly optimised HMM library exploiting repetitions in the input to speed up the forward algorithm. *BMC Bioinformatics* **14**, 339 (2013).
82. Lack, J. B. *et al.* The Drosophila Genome Nexus: A Population Genomic Resource of 623 Drosophila melanogaster Genomes, Including 197 from a Single Ancestral Range Population. *Genetics* **199**, 1229–1241 (2015).